

Time-domain multiscale shape identification in electro-sensing ^{*}

Habib Ammari[†] and Han Wang[†]

June 19, 2018

Abstract

This paper presents premier and innovative time-domain multi-scale method for shape identification in electro-sensing using pulse-type signals. The method is based on transform-invariant shape descriptors computed from filtered polarization tensors at multi-scales. The proposed algorithm enjoys a remarkable noise robustness even with far-field measurements at very limited angle of view. It opens a door for pulsed imaging using echolocation and induction data.

Mathematics Subject Classification (MSC2000): 35R30, 35B30

Keywords: weakly electric fish, electrolocation, shape classification, spectral induced polarization, location search, pulse-type signal

1 Introduction

Weakly electric fish orient themselves at night in complete darkness by employing their active electrolocation system. They generate a stable, high-frequency, weak electric field and perceive the transdermal potential modulations caused by a nearby target with different electromagnetic properties than the surrounding water [12, 15, 18, 26]. Depending on the waveform of the source (*i.e.* the electric organ discharge) which is a result of the evolution and is adapted to the habitat, weakly electric fish can be classified into the wave-type and the pulse-type [12]. The first emit a sinusoidal-like signal while the second emit brief pulses. Both types of fish have to solve the electro-sensing problem: locate the target and identify its shape and electromagnetic parameters given the current distribution over the skin. Due to the fundamental ill-posedness character of this imaging problem, it is very intriguing to see how much information weakly electric fish are able to recover [13, 14, 16, 17, 19, 20, 25, 21, 22, 23, 24].

A solution to the electric-sensing problem relies on differential imaging, *i.e.*, by forming an image from the perturbations of the field due to targets, and physics-based classification. The electric field due to the target is a complicated highly nonlinear function of its shape,

^{*}This work was supported by ERC Advanced Grant Project MULTIMOD-267184.

[†]Department of Mathematics and Applications, Ecole Normale Supérieure, 45 Rue d'Ulm, 75005 Paris, France (habib.ammari@ens.fr, han.wang@ens.fr).

electromagnetic parameters, and distance from the fish. Differential imaging helps us to understand analytically the electric sense of the weakly electric fish.

In a recent paper [1] a mathematical model of the fish has been established. Based on this model, a multifrequency shape recognition algorithm for wave-type fish has been proposed in [4]. To summarize, the wave-type fish would first locate the target using a specific frequency-space location search algorithm. Then it could extract, from the perturbations of the electric field, the polarization tensors of the target at multiple frequencies. The material parameters of the target can be computed from these extracted features. Finally, the fish might classify a target by comparing normalized singular values of the polarization tensors with those of a set of learned shapes. These geometric features extracted from the data are invariant under rigid motions and scaling of the target and therefore, they yield shape descriptors which allow the comparison and identification of the target in a dictionary of shapes.

In this paper, we study the problem of shape identification using pulse-type signals. Compared to previous investigations on wave-type electro-sensing, the present model is more complex and appears to be more realistic since shape identification performs much better even with a limited-view aspect and highly noisy data.

The overall procedure of electro-sensing is similar to the wave-type electro-sensing described above. However, unlike the wave-type electro-sensing where the solution of the forward problem in the frequency domain is separable and can be treated independently for each frequency, the shape identification problem using pulse-type signals has to be treated directly in the time domain hence is more challenging. On the other hand, the pulse-type signal contains more information from a frequency point of view and is expected to give a better performance than wave-type signals in shape identification.

The paper is organized as follows. We first introduce some notation. Then in section 2 we establish a simplified electro-sensing model in the time domain. Section 3 gives the representation of the solution. Section 4 is to formulate an asymptotic expansion of the perturbed field which allows the reconstruction of the filtered generalized polarization tensors (GPTs) from data.

Based on the polarization tensor, a time domain multi-scale shape descriptor is introduced in section 5 and its performance is analyzed through numerical experiments in section 6. The paper ends with a few concluding remarks.

Throughout this paper, we denote by Γ the fundamental solution of the Laplacian in \mathbb{R}^d with $d = 2, 3$, which satisfies $\Delta\Gamma = \delta_0$ (where δ_0 is the Dirac function at the origin) and is given by

$$\Gamma(x) := \begin{cases} \frac{1}{2\pi} \log|x|, & d = 2, \\ -\frac{1}{4\pi} \frac{1}{|x|}, & d = 3. \end{cases} \quad (1)$$

For a Banach space X equipped with the norm $\|\cdot\|_X$, we define the Schwartz space $\mathcal{S}(\mathbb{R}; X)$ as follows

$$\mathcal{S}(\mathbb{R}; X) := \{\phi : \mathbb{R} \rightarrow X \text{ is } \mathcal{C}^\infty, \text{ and } p_{a,b}(\phi) < \infty, \forall a, b \in \mathbb{N}\}, \quad (2)$$

where the semi norms $p_{a,b}$ for $a, b \in \mathbb{N}$ are defined as

$$p_{a,b}(\phi) = \sup_{t \in \mathbb{R}} |t|^a \|\phi^{(b)}(t)\|_X. \quad (3)$$

We denote by $\mathcal{S}'(\mathbb{R}; X)$ the space of tempered distributions. The Fourier transform defined as $\hat{\phi}(\omega) = \int_{\mathbb{R}} \phi(t) e^{-it\omega} dt$ for a function of $\mathcal{S}'(\mathbb{R}; X)$ is always carried out on the time variable t , and for a distribution of $\mathcal{S}'(\mathbb{R}; X)$ it is defined by the duality. In both cases the Fourier transform is a homeomorphism on the corresponding space.

We denote $L^2(\mathbb{R}_+; X)$ the space of square integrable functions $\phi : \mathbb{R}_+ \rightarrow X$, and equip it with the norm

$$\|\phi\|_{L^2(\mathbb{R}_+; X)} := \left(\int_{\mathbb{R}_+} \|\phi(t)\|_X^2 dt \right)^{1/2}, \quad (4)$$

Similarly, we denote $H^1(\mathbb{R}_+; X)$ the space of all $\phi \in L^2(\mathbb{R}_+; X)$ such that the weak derivative $\partial_t \phi \in L^2(\mathbb{R}_+; X)$ and equip it with the norm

$$\|\phi\|_{H^1(\mathbb{R}_+; X)} := \left(\|\phi\|_{L^2(\mathbb{R}_+; X)}^2 + \|\phi'\|_{L^2(\mathbb{R}_+; X)}^2 \right)^{1/2}. \quad (5)$$

Throughout the paper we will write interchangeably $\phi'(t, x)$ and $\partial_t \phi(t, x)$ for the derivative in the time variable t (similarly $\hat{\phi}'(\omega, x)$ and $\partial_\omega \hat{\phi}(\omega, x)$ for the derivative in the frequency variable ω for the Fourier transform of ϕ). We call a function ϕ *causal* if $\phi(t) = 0$ for $t < 0$. Particularly, $\phi \in \mathcal{S}'(\mathbb{R}; X)$ being causal implies $\phi^{(k)}(0) = 0$ for any $k \geq 0$.

2 Electro-sensing model

We consider in this paper the electro-sensing problem in the free space \mathbb{R}^d with point sources and receivers, which is easier to analyse compared to the complete model of fish established in [1, 4]. Before proceeding to the results of existence and uniqueness of the solution as well as its representation, we want to insist on the fact that the same type of results can be established in a similar way for the model of [1], in particular the shape identification algorithm discussed in section 5 remains unchanged and applies to any model as long as the same feature is extracted.

A target D is an open bounded set in \mathbb{R}^d , $d = 2, 3$, of class $\mathcal{C}^{1,\alpha}$, $0 < \alpha < 1$, and we can represent it as $D = z + \delta B$, where B is the reference domain of size 1 containing the origin, $\delta \ll 1$ is the characteristic size of D , and z is its location. The characteristic function of D is denoted by χ_D , and its constant conductivity and permittivity are denoted by σ and ε respectively with $\sigma > 0, \varepsilon > 0$. The conductivity and permittivity distributions of the whole space are piecewise constant:

$$\sigma(x) = \sigma_0 + (\sigma - \sigma_0)\chi_D(x), \quad \text{and} \quad \varepsilon(x) = \varepsilon_0 + (\varepsilon - \varepsilon_0)\chi_D(x) \quad (6)$$

where $\sigma_0 > 0, \varepsilon_0 \geq 0$ and $\sigma_0 \neq \sigma, \varepsilon_0 \neq \varepsilon$ are the background values and χ_D is the characteristic function of D .

2.1 Governing equation for the voltage potential

Under the electro-quasi-static (or EQS) approximation of the Maxwell's system, the electric field reads $E(t, x) = \nabla u(t, x)$, where u is the voltage potential, and the magnetic field H

satisfies

$$\nabla \times H(t, x) = \varepsilon(x)\partial_t E(t, x) + J(t, x), \quad (7)$$

where the current density $J(t, x) = \sigma(x)E(t, x) + J_s(t, x)$, *i.e.* the sum of induction and source current. Let $f(t, x) := -\nabla \cdot J_s(t, x)$ be the source. Taking the divergence of (7), we get

$$\nabla \cdot (\sigma(x)E(t, x) + \varepsilon(x)\partial_t E(t, x)) = -\nabla \cdot J_s(t, x) = f(t, x),$$

or in terms of u ,

$$\nabla \cdot (\sigma(x) + \varepsilon(x)\partial_t)\nabla u(t, x) = f(t, x). \quad (8)$$

We complete (8) by a decay condition at infinity as well as an initial condition at $t = 0$, and obtain the governing equation of the voltage potential

$$\begin{cases} \nabla \cdot (\sigma(x) + \varepsilon(x)\partial_t)\nabla u(t, x) = f(t, x) & \text{in } \mathbb{R}_+ \times \mathbb{R}^d, \\ |u(t, x)| = O(|x|^{1-d}) & \text{as } |x| \rightarrow +\infty, t \in \mathbb{R}_+, \\ u(0, x) = u_0(x) & \text{in } \mathbb{R}^d. \end{cases} \quad (9)$$

For the eletro-sensing problem in water we typically set for the surrounding water $\sigma_0 = 1$ and $\varepsilon_0 = 0$. Furthermore, we suppose there is no potential at the initial state and let $\overline{D}^c = \mathbb{R}^d \setminus \overline{D}$. Under these settings, it is easy to see that (9) can be rewritten as the following transmission problem:

$$\begin{cases} \varepsilon \Delta u'(t) + \sigma \Delta u(t) = 0 & \text{in } \mathbb{R}_+ \times D, \\ \Delta u(t) = f(t) & \text{in } \mathbb{R}_+ \times \overline{D}^c, \\ u(t)|_{-} = u(t)|_{+} & \text{on } \mathbb{R}_+ \times \partial D, \\ \varepsilon \frac{\partial u'(t)}{\partial \nu}|_{-} + \sigma \frac{\partial u(t)}{\partial \nu}|_{-} = \frac{\partial u(t)}{\partial \nu}|_{+} & \text{on } \mathbb{R}_+ \times \partial D, \\ |u(t, x)| = O(|x|^{1-d}) & \text{as } |x| \rightarrow +\infty, t \in \mathbb{R}_+, \\ u(0, x) = 0 & \text{in } \mathbb{R}^d. \end{cases} \quad (10)$$

2.1.1 Uniqueness of a solution to the governing equation

We define the Banach spaces

$$X = H_{\text{loc}}^1(\mathbb{R}^d), \quad X' = H^{-1}(\mathbb{R}^d), \quad (11)$$

and consider (9) in $H^1(\mathbb{R}_+; X)$ with the initial condition $u_0 \in X$, and the source term $f \in H^1(\mathbb{R}_+; X')$.

Lemma 2.1. *If the solution to (9) fulfills $u \in H^1(\mathbb{R}_+; X)$, then it is unique.*

Proof. We introduce two bilinear forms

$$a_1(u, v) = \int_{\mathbb{R}^d} \varepsilon(x) \nabla u(x) \cdot \nabla v(x) dx, \quad a_2(u, v) = \int_{\mathbb{R}^d} \sigma(x) \nabla u(x) \cdot \nabla v(x) dx. \quad (12)$$

Let u_1, u_2 be two solutions to (9) in $H^1(\mathbb{R}_+; X)$. Then, their difference $w = u_1 - u_2 \in H^1(\mathbb{R}_+; X)$ must solve

$$\begin{cases} \nabla \cdot (\sigma(x) + \varepsilon(x) \partial_t) \nabla w(t, x) = 0, & \text{in } \mathbb{R}_+ \times \mathbb{R}^d, \\ |w(t, x)| = O(|x|^{1-d}), & \text{as } |x| \rightarrow +\infty, t \in \mathbb{R}_+, \\ w(0, x) = 0, & \text{in } \mathbb{R}^d. \end{cases} \quad (13)$$

Multiplying the first line by a test function $\varphi \in \mathcal{C}_0^\infty(\mathbb{R}^d)$ and integrating by parts in \mathbb{R}^d yield:

$$a_1(w(t), \varphi) + a_2(w'(t), \varphi) = 0, \quad \text{for a.e. } t \in \mathbb{R}_+.$$

which implies, by the density of $\mathcal{C}_0^\infty(\mathbb{R}^d)$ in $H^1(\mathbb{R}^d)$,

$$a_1(w'(t), w(t)) + a_2(w(t), w(t)) = 0, \quad \text{for } t \in \mathbb{R}_+ \text{ a.e.}$$

For any $T > 0$, integrating the expression above on $[0, T]$ and using the initial condition $\nabla w(0, x) = 0$ gives

$$\frac{1}{2} \int_{\mathbb{R}^d} \varepsilon(x) |\nabla w'(T)|^2 dx + \int_{\mathbb{R}^d} \sigma(x) \int_0^T |\nabla w(t)|^2 dt dx = 0,$$

which means, since $\sigma(x) > 0$ and $\varepsilon(x) \geq 0$, that $|\nabla w(t, x)|^2 = 0$ in $[0, T] \times \mathbb{R}^d$. Since $T > 0$ is arbitrary, combining this with the decay condition in (13) implies $u_1(t, x) = u_2(t, x)$ a.e. in $\mathbb{R}_+ \times \mathbb{R}^d$. □

2.2 Electric organ and pulse-type signals

The time-varying source current f emitted by the fish can be modeled as

$$f(t, x) = h(t) \tilde{f}(x), \quad (14)$$

with h being the shape form (*i.e.* the time profile) of the source. \tilde{f} is a function modeling the electric organ:

$$\tilde{f}(x) = \sum_{j=1}^p a_j \delta_0(x - x_s^j) \quad \text{with } x_s^j \in \overline{D}^c, \quad (15)$$

where $x_s^j \in \mathbb{R}^d, j = 1 \dots p$ are the point sources and characterize the spatial distribution of the electric organ, and a_j fulfills the neutrality condition:

$$\sum_{j=1}^p a_j = 0, \quad (16)$$

which insures the decay behavior $|u(t, x)| = O(|x|^{1-d})$ at infinity.

We refer the reader to [1] for more details on the modeling of the electric organ and [4] for the electrolocation using wave-type signals. Throughout this paper, we will consider the pulse shape form h under the assumption

$$h \text{ is causal and } h \in \mathcal{S}(\mathbb{R}), \quad (17)$$

where $\mathcal{S}(\mathbb{R})$ is the classical Schwartz space. As a simple consequence it holds $h^{(k)}(0) = 0$ for any $k \geq 0$.

It is worth emphasizing that causality is important issue because of physical considerations. Throughout this paper, we will carefully check that the solution to the electro-sensing problem is causal.

3 Representation of solution

We introduce in this section an integral representation of the solution of the problem (10). The following notation will be used in this section. Let

$$\kappa(\omega) := \sigma + i\varepsilon\omega, \quad \lambda(\omega) := \frac{\kappa(\omega) + 1}{2(\kappa(\omega) - 1)}, \quad \lambda := \frac{\sigma + 1}{2(\sigma - 1)}, \quad \alpha := \frac{\varepsilon}{\sigma - 1}. \quad (18)$$

We call $\kappa(\omega)$ the admittivity.

3.1 Layer potentials

Let the single layer potential of a density $\phi \in L^2(\partial D)$ be defined by

$$\mathcal{S}_D[\phi](x) := \int_{\partial D} \Gamma(x - y)\phi(y) ds(y), \quad x \in \mathbb{R}^d. \quad (19)$$

It is well-known that $\mathcal{S}_D[\phi]$ is harmonic on $\mathbb{R}^d \setminus \partial D$. Let Neumann-Poincaré operator \mathcal{K}_D^* on $L^2(\partial D)$ be given by

$$\mathcal{K}_D^*[\phi](x) := \int_{\partial D} \frac{\partial \Gamma}{\partial \nu(x)}(x - y)\phi(y) ds(y), \quad \phi \in L^2(\partial D). \quad (20)$$

Then we have the jump formula for the single layer potential:

$$\frac{\partial \mathcal{S}_D[\phi]}{\partial \nu} \Big|_{\pm} = \left(\pm \frac{1}{2}I + \mathcal{K}_D^* \right) [\phi]. \quad (21)$$

We also introduce the L^2 -adjoint of \mathcal{K}_D^* , \mathcal{K}_D , which is given by

$$\mathcal{K}_D[\phi](x) := \int_{\partial D} \frac{\partial \Gamma}{\partial \nu(y)}(x - y)\phi(y) ds(y), \quad \phi \in L^2(\partial D).$$

3.2 Preliminary results

We recall first that the operator \mathcal{K}_D^* is compact, provided that D is of class $\mathcal{C}^{1,\alpha}$ for some $0 < \alpha < 1$, with eigenvalues included in $(-\frac{1}{2}, \frac{1}{2}]$ and it can be decomposed as [8]

$$\mathcal{K}_D^* [\phi] = \sum_{j=1}^{\infty} \mu_j \langle \phi, u_j \rangle_s u_j, \quad (22)$$

where μ_j and $u_j \in L^2(\partial D)$ are the j -th eigenvalue and eigenvector of \mathcal{K}_D^* respectively, and the scalar product

$$\langle \phi, u_j \rangle_s := \int_{\partial D} \phi(y) \mathcal{S}_D [u_j] (y) d\sigma(y). \quad (23)$$

Furthermore, we have the the energy identity

$$\|\hat{\phi}\|_{L^2(\partial D)}^2 = \sum_j |\langle \hat{\phi}, u_j \rangle_s|^2. \quad (24)$$

The spectral decomposition (22) is based on a Calderón's identity and a symmetrization principle; see for instance [8, Chap. 2].

Lemma 3.1. *Let $\varphi \in \mathcal{S}(\mathbb{R}; L^2(\partial D))$ and let $\hat{\varphi}$ be its Fourier Transform. The mapping*

$$\hat{\varphi}(\omega) \mapsto (\lambda(\omega)I - \mathcal{K}_D^*) [\hat{\varphi}(\omega)], \quad \forall \omega \in \mathbb{R} \quad (25)$$

defines a homeomorphism on $\mathcal{S}(\mathbb{R}; L^2(\partial D))$, and in particular,

$$\hat{\varphi} \xrightarrow{\mathcal{S}} 0 \text{ implies } (\lambda(\omega)I - \mathcal{K}_D^*)^{-1} [\hat{\varphi}] \xrightarrow{\mathcal{S}} 0. \quad (26)$$

The same results hold also for the operator $(\lambda(\omega)I - \mathcal{K}_D)$.

Proof. We shall prove the lemma only for $(\lambda(\omega)I - \mathcal{K}_D^*)$. The case of the operator $(\lambda(\omega)I - \mathcal{K}_D)$ is similar.

For $b \in \mathbb{N}$, let $\lambda^{(b)}(\omega)$ be the derivative of order b of $\lambda(\omega)$ in ω , then any $\hat{\varphi} \in \mathcal{S}(\mathbb{R}; L^2(\partial D))$ multiplied by $\lambda^{(b)}(\omega)$ remains a function of $\mathcal{S}(\mathbb{R}; L^2(\partial D))$. Moreover, by applying the product rule and the boundedness of \mathcal{K}_D^* , it is easy to verify

$$p_{a,b}((\lambda(\omega)I - \mathcal{K}_D^*) [\hat{\varphi}]) \lesssim \sum_{0 \leq b' \leq b} p_{a,b'}(\hat{\varphi}) < \infty, \quad \forall a, b \in \mathbb{N}$$

and hence, $(\lambda(\omega)I - \mathcal{K}_D^*) [\hat{\varphi}] \in \mathcal{S}(\mathbb{R}; L^2(\partial D))$ for any $\hat{\varphi} \in \mathcal{S}(\mathbb{R}; L^2(\partial D))$.

For a fixed ω , the operator $(\lambda(\omega)I - \mathcal{K}_D^*)$ is invertible on $L^2(\partial D)$. Hence

$$(\lambda(\omega)I - \mathcal{K}_D^*) [\hat{\varphi}] = 0, \quad \forall \omega \in \mathbb{R}$$

implies $\hat{\varphi}(\omega) = 0, \forall \omega$, thus $\hat{\varphi} = 0$ in $\mathcal{S}(\mathbb{R}; L^2(\partial D))$. Therefore $(\lambda(\omega)I - \mathcal{K}_D^*)$ is injective.

To prove that $(\lambda(\omega)I - \mathcal{K}_D^*)$ is surjective, it suffices to show that $(\lambda(\omega)I - \mathcal{K}_D^*)^{-1}$ maps $\mathcal{S}(\mathbb{R}; L^2(\partial D))$ to $\mathcal{S}(\mathbb{R}; L^2(\partial D))$. The following statement can be verified easily. For $k \in \mathbb{N}$, we have

$$\left((\lambda(\omega)I - \mathcal{K}_D^*)^{-k} [\hat{\varphi}] \right)' = (\lambda(\omega)I - \mathcal{K}_D^*)^{-k} [\hat{\varphi}'] - k\lambda'(\omega)(\lambda(\omega)I - \mathcal{K}_D^*)^{-(k+1)} [\hat{\varphi}], \quad \forall \omega \in \mathbb{R},$$

and more generally,

$$\left((\lambda(\omega)I - \mathcal{K}_D^*)^{-1} [\hat{\varphi}] \right)^{(b)} = \sum_{0 \leq b' \leq b+1} (\lambda(\omega)I - \mathcal{K}_D^*)^{-b'} [P_{b'}(\hat{\varphi}(\omega); \lambda(\omega))]$$

where $P_{b'}$ is a differential operator of order $b+1$ in ω with coefficients depending on $\lambda(\omega)$ and its derivatives (up to order $b+1$). Furthermore,

$$\|(\lambda(\omega)I - \mathcal{K}_D^*)^{-1}\|_{L^2(\partial D)} \leq \frac{1}{|\lambda(\omega)| - 1/2}$$

which behaves as $O(|\omega|)$ only when $\omega \rightarrow \infty$, therefore it holds

$$p_{a,b} \left((\lambda(\omega)I - \mathcal{K}_D^*)^{-1} [\hat{\varphi}] \right) \lesssim \sum_{0 \leq a', b' \leq a+b+1} p_{a', b'}(\hat{\varphi}) < \infty, \quad \forall a, b \in \mathbb{N}$$

Hence $(\lambda(\omega)I - \mathcal{K}_D^*)$ is surjective.

Finally, the claim (26) follows from the inequality above and this completes the proof. \square

The following result shows that the operator $(\lambda(\omega)I - \mathcal{K}_D^*)^{-1}$ can preserve causality, at least for some special class of functions such as separable functions: $\psi(t, x) = h(t)\tilde{\psi}(x)$ for some function h of the classical Schwartz space $\mathcal{S}(\mathbb{R})$ and $\tilde{\psi}$ of $L_0^2(\partial D)$. Here, $L_0^2(\partial D)$ is the set of functions in $L^2(\partial D)$ with zero mean-value.

Theorem 3.2. *For a separable and causal function $\psi \in \mathcal{S}(\mathbb{R}; L_0^2(\partial D))$, define a function φ in the frequency domain as*

$$\hat{\varphi} = (\lambda(\omega)I - \mathcal{K}_D^*)^{-1} [\hat{\psi}]. \quad (27)$$

Then $\varphi \in \mathcal{S}(\mathbb{R}; L_0^2(\partial D))$ and φ is causal.

Proof. The fact that $\varphi \in \mathcal{S}(\mathbb{R}; L_0^2(\partial D))$ follows from Lemma 3.1 and the property that $(\lambda(\omega)I - \mathcal{K}_D^*)$ is a bijection on $L_0^2(\partial D)$.

For fixed ω , the singular value decomposition gives:

$$\hat{\varphi}(\omega) = (\lambda(\omega)I - \mathcal{K}_D^*)^{-1} [\hat{\psi}(\omega)] = \sum_j \frac{\langle \hat{\psi}, u_j \rangle_{\mathcal{S}}}{\lambda(\omega) - \mu_j} u_j \quad (28)$$

where $|\mu_j| < \frac{1}{2}$ and $u_j \in L_0^2(\partial D)$ are the j -th eigenvalue and eigenvector of \mathcal{K}_D^* respectively and are independent of ω . Notice that

$$\frac{1}{\lambda(\omega) - \mu_j} = \alpha_j \left(1 - \frac{\beta_j}{\gamma_j + i\omega} \right),$$

with the constants $\alpha_j = \frac{2}{1-2\mu_j}$, $\beta_j = \alpha_j/\varepsilon$ and $\gamma_j = \sigma/\varepsilon + \frac{1+2\mu_j}{\varepsilon(1-2\mu_j)} > 0$. Let

$$g_j(t) = \mathbb{1}_{t \geq 0}(t)e^{-\gamma_j t}, \quad (29)$$

whose Fourier transform is $\hat{g}_j(\omega) = 1/(\gamma_j + i\omega)$. Then the function $(\lambda(\omega) - \mu_j)^{-1}\hat{\psi}(\omega)$ in the time domain is

$$\alpha_j\psi(t) - \alpha_j\beta_j g_j * \psi(t),$$

which is clearly a causal function. Hence it suffices to show that the sum in (28) converges in $\mathcal{S}(\mathbb{R}; L^2(\partial D))$. Then by taking inverse Fourier transform term by term we obtain the causality of φ . For doing so, we write for given $a, b \in \mathbb{N}$

$$\begin{aligned} \left(p_{a,b} \left(\sum_{j=N}^{\infty} \frac{\langle \hat{\psi}, u_j \rangle_s}{\lambda(\omega) - \mu_j} u_j \right) \right)^2 &= \sup_{\omega \in \mathbb{R}} |\omega|^{2a} \left\| \sum_{j=N}^{\infty} \left(\frac{\langle \hat{\psi}, u_j \rangle_s}{\lambda(\omega) - \mu_j} \right)^{(b)} u_j \right\|_{L^2(\partial D)}^2 \\ &= \sup_{\omega \in \mathbb{R}} |\omega|^{2a} \sum_{j=N}^{\infty} \left| \left(\frac{\langle \hat{\psi}, u_j \rangle_s}{\lambda(\omega) - \mu_j} \right)^{(b)} \right|^2, \end{aligned}$$

where the b -th order derivative in the first identity is taken termwise since the derivative is a continuous linear mapping on $\mathcal{S}(\mathbb{R}; L^2(\partial D))$. It is easy to see that it will be bounded for any $a, b \in \mathbb{N}$ if

$$\sup_{\omega \in \mathbb{R}} |\omega|^{2a} \sum_{j=N}^{\infty} \left| \langle \hat{\psi}^{(b)}, u_j \rangle_s \right|^2 < \infty, \quad \forall a, b \in \mathbb{N},$$

which is indeed the case since $\psi(t, x) = h(t)\tilde{\psi}(x)$ with $h \in \mathcal{S}(\mathbb{R})$ and $\tilde{\psi} \in L_0^2(\partial D)$. Moreover due to the energy identity (24), the last expression tends to 0 as $N \rightarrow \infty$. This proves the convergence of (28) in $\mathcal{S}(\mathbb{R}; L^2(\partial D))$. The proof of the theorem is then complete. \square

3.3 Integral representation and an existence result

We denote in the following

$$U(t, x) = h(t)\tilde{U}(x) = h(t) \sum_{j=1}^p a_j \Gamma(x - x_s^j), \quad (30)$$

which is a solution to $\Delta U(t, x) = h(t)\tilde{f}(x) = f(t, x)$ and decays as $O(|x|^{1-d})$ when $|x|$ goes to infinity, due to condition (16).

Theorem 3.3. *Let $\alpha, \lambda, \lambda(\omega)$ be defined as in (18). For the source term (14) with h fulfilling (17), the unique solution to (10) is given by*

$$u(t) = U(t) + \mathcal{S}_D[\varphi(t)], \quad (31)$$

where $\varphi \in \mathcal{S}(\mathbb{R}; L_0^2(\partial D))$ is causal and solves the following equation:

$$(\lambda I - \mathcal{K}_D^*) [\varphi] + \alpha \left(\frac{1}{2} I - \mathcal{K}_D^* \right) [\varphi'] = (1 + \alpha \partial_t) \frac{\partial U}{\partial \nu}, \quad (32)$$

or equivalently in the frequency domain

$$(\lambda(\omega) I - \mathcal{K}_D^*) [\hat{\varphi}] = \frac{\partial \hat{U}}{\partial \nu}. \quad (33)$$

Furthermore, the solution (31) is causal and belongs to $H^1(\mathbb{R}_+; X)$.

Proof. For u given by (31), one can check easily that the first and second identities in (10) are verified. Further, since U and $\mathcal{S}_D[\varphi(t)]$ are both continuous across the boundary, the third identity also holds true. The fourth identity in (10) is equivalent to

$$\varepsilon \left(\frac{\partial}{\partial \nu} \mathcal{S}_D[\varphi] \right)' \Big|_- + \sigma \left(\frac{\partial}{\partial \nu} \mathcal{S}_D[\varphi] \right) \Big|_- - \left(\frac{\partial}{\partial \nu} \mathcal{S}_D[\varphi] \right) \Big|_+ = (1 - \sigma) \frac{\partial U}{\partial \nu} - \varepsilon \frac{\partial U'}{\partial \nu},$$

which becomes (32) by applying the jump formula (21) and by interchanging the derivative and the single layer potential. Taking Fourier transform in the t -variable in (32) yields (33) after some simplifications.

In the time domain, the term on the right-hand side of (33) corresponds to $h(t) \frac{\partial \tilde{U}(x)}{\partial \nu}$ which is separable, causal, and belongs to $\mathcal{S}(\mathbb{R}; L_0^2(\partial D))$. Therefore by Corollary 3.2 the function $\varphi \in \mathcal{S}(\mathbb{R}; L_0^2(\partial D))$ is causal. This proves the causality of the solution u , as well as the fifth identity in (10), since $\mathcal{S}_D[\varphi(t)]$ decays as $O(|x|^{1-d})$ for $\varphi(t)$ being an $L_0^2(\partial D)$ function.

Finally, $\varphi \in \mathcal{S}(\mathbb{R}; L_0^2(\partial D))$ being causal implies $\varphi(0) = 0$ so the last identity in (10) is also fulfilled.

It is clear that $U \in H^1(\mathbb{R}_+; X)$. To prove $u \in H^1(\mathbb{R}_+; X)$, it suffices to show for any compact $K \subset \mathbb{R}^d$ the boundness of:

$$I_1 + I_2 = \int_{\mathbb{R}_+} \|\mathcal{S}_D[\varphi(t)]\|_{H^1(K)}^2 dt + \int_{\mathbb{R}_+} \|\mathcal{S}_D[\varphi'(t)]\|_{H^1(K)}^2 dt. \quad (34)$$

Note that

$$I_1 = \int_{\mathbb{R}_+} \int_K |\mathcal{S}_D[\varphi(t)](x)|^2 dx + \int_{\mathbb{R}_+} \int_K |\nabla \mathcal{S}_D[\varphi(t)](x)|^2 dx,$$

and the first term in I_1 can be estimated as

$$\int_{\mathbb{R}_+} \int_K \left| \int_{\partial D} \Gamma(x-y) \varphi(t, y) d\sigma(y) \right|^2 dx dt \leq \int_{\mathbb{R}_+} \int_K \|\Gamma(x-\cdot)\|_{L^2(\partial D)}^2 \|\varphi(t)\|_{L^2(\partial D)}^2 dx dt$$

and is bounded since the singularity of Γ is integrable and φ is a function of $\mathcal{S}(\mathbb{R}; L_0^2(\partial D))$. Similarly one can prove the boundedness for the other terms, therefore $u \in H^1(\mathbb{R}_+; X)$.

The uniqueness of the expression is a consequence of Lemma 2.1 and then the well-posedness of (10) is now established. \square

4 Time-dependent GPTs and asymptotic expansions

In this section we extend the concept of generalized polarization tensor (GPT) to the time domain¹. The GPTs will be the features of the target to be recovered from measurements. For the sake of simplicity, we only discuss the two-dimensional case here. The three-dimensional case can be treated by following the same approach as in [7].

For the domain D and the order $m, n \in \mathbb{N}$, the GPT in the frequency domain (at the frequency ω) is a 2×2 matrix of the following form [2]

$$\hat{\mathbf{M}}_{mn} = \hat{\mathbf{M}}_{mn}(\omega; D) = \begin{pmatrix} \hat{M}_{mn}^{cc} & \hat{M}_{mn}^{cs} \\ \hat{M}_{mn}^{sc} & \hat{M}_{mn}^{ss} \end{pmatrix}, \quad (35)$$

where \hat{M}_{mn}^{cs} is defined as

$$\hat{M}_{mn}^{cs}(\omega; D) = \int_{\partial D} S_n(y) (\lambda(\omega)I - \mathcal{K}_D^*)^{-1} \left[\frac{\partial C_m}{\partial \nu} \right] (y) d\sigma(y) \quad (36)$$

with C_m and S_m being respectively the real and imaginary parts of the harmonic polynomial $(x_1 + ix_2)^m$, and $\lambda(\omega)$ being defined as in (18). The other terms \hat{M}_{mn}^{cc} , \hat{M}_{mn}^{sc} , \hat{M}_{mn}^{ss} in (35) are defined in a similar way, by replacing the symbols c and s by the corresponding polynomials C_m (or C_n) and S_m (or S_n) respectively. The time-dependent GPTs $\mathbf{M}_{mn}(t; D)$ is also a 2×2 matrix consisting of the inverse Fourier transform (in the sense of distribution) of each term of $\hat{\mathbf{M}}_{mn}(\omega; D)$.

In the following we denote by $\hat{\mathbf{M}} = \hat{\mathbf{M}}(\omega; D) = (\hat{\mathbf{M}}_{mn})_{mn}$ the block matrix of the GPTs in the frequency domain, and $\mathbf{M} = \mathbf{M}(t; D) = (\mathbf{M}_{mn})_{mn}$ in the time domain.

4.1 Properties of the time-dependant GPTs

The operator $(\lambda(\omega)I - \mathcal{K}_D^*)^{-1}$ is uniformly continuous in ω with respect to the operator norm $\|\cdot\|_{L^2(\partial D)}$, and converges to $(\frac{1}{2}I - \mathcal{K}_D^*)^{-1}$ as ω tends to infinity. In the limit case, $\hat{\mathbf{M}}_{mn}$ becomes independent of the frequency but remains well defined since $(\frac{1}{2}I - \mathcal{K}_D^*)$ is invertible on $L^2_0(\partial D)$. Hence we obtain the following result.

Proposition 4.1. *For any $m, n \in \mathbb{N}$ and as a function of ω , each entry of $\hat{\mathbf{M}}_{mn}(\omega; D)$ is uniformly continuous and bounded. Furthermore,*

$$\lim_{|\omega| \rightarrow \infty} \hat{\mathbf{M}}_{mn}(\omega; D) = \hat{\mathbf{M}}_{mn}(\infty; D),$$

where $\hat{\mathbf{M}}_{mn}(\infty; D)$ is some well-defined matrix.

GPT as distribution For a general shape D its GPT $\hat{\mathbf{M}}_{mn}(\omega; D)$ does not exhibits any decay as ω tends to infinity, and we interpret the time domain \mathbf{M}_{mn} as a distribution in $\mathcal{S}'(\mathbb{R})$. Furthermore, the entries of $\hat{\mathbf{M}}_{mn}$ are L^1_{loc} functions, so we define the action of M_{mn}^{cs} in the frequency domain as

$$\langle \hat{M}_{mn}^{cs}, \varphi \rangle_{\mathcal{S}', \mathcal{S}} := \int_{\mathbb{R}} \varphi(\omega) \hat{M}_{mn}^{cs}(\omega) d\omega \quad (37)$$

and similarly for the other entries M_{mn}^{cc} , M_{mn}^{sc} , and M_{mn}^{ss} .

¹The GPT as it is defined in this paper is actually the so-called *contracted* GPT introduced in [10].

Proposition 4.2. *The distribution $\mathbf{M}_{mn}(t; D) \in \mathcal{S}'(\mathbb{R})$ is causal, which means that for any causal function $\varphi \in \mathcal{S}(\mathbb{R})$,*

$$\langle \mathbf{M}_{mn}, \tilde{\varphi} \rangle_{\mathcal{S}', \mathcal{S}} = 0, \quad \text{where } \tilde{\varphi}(t) := \varphi(-t), \quad (38)$$

holds.

Proof. We prove the result for M_{mn}^{cs} only. The result for the other entries can be proved similarly. By Fourier transform of the distribution we have

$$2\pi \langle M_{mn}^{cs}, \tilde{\varphi} \rangle_{\mathcal{S}', \mathcal{S}} = \langle \hat{M}_{mn}^{cs}, \hat{\varphi} \rangle_{\mathcal{S}', \mathcal{S}},$$

and by (37),

$$\langle \hat{M}_{mn}^{cs}, \hat{\varphi} \rangle_{\mathcal{S}', \mathcal{S}} = \int_{\partial D} S_n(y) \underbrace{\int_{\mathbb{R}} (\lambda(\omega)I - \mathcal{K}_D^*)^{-1} \left[\hat{\varphi}(\omega) \frac{\partial C_m}{\partial \nu} \right] (y) d\omega}_{\hat{\psi}} d\sigma(y),$$

where the function $\hat{\varphi} \frac{\partial C_m}{\partial \nu} \in \mathcal{S}(\mathbb{R}; L_0^2(\partial D))$ in the time domain is separable and causal. By Corollary 3.2, the function $\psi \in \mathcal{S}(\mathbb{R}; L_0^2(\partial D))$ defined in the expression above via $\hat{\psi}$ is causal in the time domain, hence

$$\langle M_{mn}^{cs}, \tilde{\varphi} \rangle_{\mathcal{S}', \mathcal{S}} = \langle S_n, \psi(0) \rangle_{L^2(\partial D)} = 0,$$

due to the fact $\psi(0) = 0$. This completes the proof. \square

4.2 Asymptotic expansion

Taking the Fourier transform of the representation formula (31), it follows that

$$\hat{u}(\omega, x) = \hat{U}(\omega, x) + \mathcal{S}_D[\hat{\varphi}(\omega)](x),$$

and since $\lambda(\omega)I - \mathcal{K}_D^*$ is invertible, plugging (33) into the identity above yields

$$\hat{u}(\omega, x) = \hat{U}(\omega, x) + \hat{h}(\omega) \mathcal{S}_D \left[(\lambda(\omega)I - \mathcal{K}_D^*)^{-1} \left[\frac{\partial \tilde{U}}{\partial \nu} \right] \right] (x). \quad (39)$$

Let $z \in \mathbb{R}^d$ be an estimated position of the target D . For the source $x_s = \{x_s^1, \dots, x_s^p\}$ with $x_s^j \in \overline{D}^c$ and the receiver $x_r \in \overline{D}^c$, let (ρ_s^j, θ_s^j) and (ρ_r, θ_r) be the polar coordinate of $x_s^j - z, j = 1 \dots p$ and $x_r - z$ respectively. We introduce the 1×2 matrices

$$A_{sm} = \sum_{j=1}^p \frac{a_j}{2\pi m \rho_s^j} \begin{pmatrix} \cos(m\theta_s^j) & \sin(m\theta_s^j) \end{pmatrix}, \quad B_{rn} = \frac{1}{2\pi n \rho_r} \begin{pmatrix} \cos(n\theta_r) & \sin(n\theta_r) \end{pmatrix}. \quad (40)$$

Then by expanding the fundamental solution Γ in (39) into its Taylor series as done in [2], we can establish an asymptotic expansion relating the data with the GPTs:

$$\hat{u}(\omega, x_r) - \hat{U}(\omega, x_r) = \sum_{m,n=1}^K A_{sm} \hat{h}(\omega) \hat{\mathbf{M}}_{mn}(\omega; D - z) B_{rn}^\top + E_K, \quad (41)$$

where $D - z$ denotes the translation of D by the vector $-z$, K is the truncation order and E_K is the truncation error which decays exponentially to 0 as K increases [2].

4.3 Linear system

In the time domain, the perturbation of the field corresponding to the source x_s and recorded by the receiver x_r constitutes the (s, r) -th entry of the multi-static response (MSR) matrix $\mathbf{V}(t) = (V_{sr}(t))_{sr}$ at the time t :

$$V_{sr}(t) = u(t, x_r) - U(t, x_r), \quad (42)$$

and its Fourier transform in t is just the term on the left-hand side of (41) that we denote by $\hat{\mathbf{V}}(\omega) = (\hat{V}_{sr}(\omega))_{sr}$. By introducing a linear operator \mathbf{L} in (41) and dropping the truncation error E_K , we can rewrite it as a linear system:

$$\hat{\mathbf{V}}(\omega) \simeq \mathbf{L}(\hat{h}(\omega)\hat{\mathbf{M}}(\omega; D - z)), \quad (43)$$

where $\hat{\mathbf{M}}(\omega; D - z)$ is a $2K \times 2K$ block matrix. Remark that the operator \mathbf{L} depends only on the measurement system (*i.e.* the reference point z , the sources x_s and receivers x_r) and the truncation order, and that the data $\hat{\mathbf{V}}(\omega)$ or $\mathbf{V}(t)$ can be contaminated by some white noise.

4.3.1 Filtered GPT

By Proposition 4.2 the GPT \mathbf{M} in the time domain is a distribution, however \mathbf{M} “filtered” by h becomes a regular function. To show this we introduce the concept of *Filtered GPT*:

Definition 4.1. The filtered GPT $\mathbf{N}_{mn}(t; D)$ in the time domain is a 2×2 matrix which corresponds in the frequency domain to

$$\hat{\mathbf{N}}_{mn}(\omega; D) = \begin{pmatrix} \hat{N}_{mn}^{cc} & \hat{N}_{mn}^{cs} \\ \hat{N}_{mn}^{sc} & \hat{N}_{mn}^{ss} \end{pmatrix} = \hat{h}(\omega)\hat{\mathbf{M}}_{mn}(\omega; D). \quad (44)$$

Proposition 4.3. Let $h \in \mathcal{S}(\mathbb{R})$ be causal and the filtered GPT $\mathbf{N}_{mn}(t; D)$ defined as in Definition 4.1. Then each entry of \mathbf{N}_{mn} in the time domain is causal and belongs to $\mathcal{S}(\mathbb{R})$.

Proof. We prove this result only for the entry \hat{N}_{mn}^{cs} . By definition

$$\hat{N}_{mn}^{cs}(\omega) := \hat{h}(\omega)\hat{M}_{mn}^{cs}(\omega; D) = \int_{\partial D} S_n(y) \underbrace{(\lambda(\omega)I - \mathcal{K}_D^*)^{-1} \left[\hat{h}(\omega) \frac{\partial C_m}{\partial \nu} \right]}_{\hat{\varphi}(\omega)}(y) d\sigma(y),$$

where $\hat{\varphi}$ in time domain is causal and a function of $\mathcal{S}(\mathbb{R}; L_0^2(\partial D))$, as a consequence of Corollary 3.2. It is easy to check that the inner product $\langle S_n, \cdot \rangle_{L^2(\partial D)}$ defines a continuous linear mapping from $\mathcal{S}(\mathbb{R}; L^2(\partial D))$ to $\mathcal{S}(\mathbb{R})$, hence \hat{N}_{mn}^{cs} as well as N_{mn}^{cs} is in $\mathcal{S}(\mathbb{R})$. \square

In the following we denote the block matrix $\mathbf{N} = \mathbf{N}(t; D) = (\mathbf{N}_{mn})_{mn}$, then the linear system (43) can be rewritten in the time domain as

$$\mathbf{V}(t) \simeq \mathbf{L}(\mathbf{N}(t; D - z)). \quad (45)$$

Although the two linear systems (43) and (45) are equivalent, in practice it is preferred to consider (45) since the measurements are taken directly in the time domain. By inverting \mathbf{L} one can estimate $\mathbf{N}(t; D - z)$ from data, and the results in [2] about the maximum resolving order as well as the stability remain valid here.

Remark 4.1. Notice that one cannot expect to recover stably the GPT \mathbf{M} from the filtered GPT \mathbf{N} by a deconvolution procedure, since the pulse-type signal h in practice is always band-limited, while in general \mathbf{M} is not band-limited function, as shown in Proposition 4.1.

5 Shape identification with pulse-type signals

We aim to identify a target D from a dictionary of reference shapes $\{B_1 \dots B_N\}$ up to some rigid transformation and dilation. In this section we propose a time domain multi-scale method for shape identification. For the sake of simplicity, we assume that the target and all reference shapes have the same physical parameters σ, ε , which can be estimated from data via a nonlinear parameter fitting procedure as described in [1].

5.1 Invariant properties of the filtered GPTs

In [2] and [4] the properties of the GPTs $\hat{\mathbf{M}}(\omega; D)$ with respect to the scaling and rigid motion have been investigated. The filtered GPTs $\mathbf{N}(t; D)$ being defined in the frequency domain as $\hat{\mathbf{N}}(\omega; D) = \hat{h}(\omega)\hat{\mathbf{M}}(\omega; D)$ inherit naturally all of these properties. The following result is a direct consequence of the results in [2] and [4] and its proof is skipped here.

Proposition 5.1. *The matrix of the filtered GPTs $\mathbf{N}(t; D)$ is symmetric. Moreover, for arbitrary $z \in \mathbb{R}^d$, $s > 0$ and $R \in SO(\mathbb{R}^d)$, with $SO(\mathbb{R}^d)$ being the rotation group in \mathbb{R}^d , the following identity holds for the $d \times d$ square matrix \mathbf{N}_{11} :*

$$\mathbf{N}_{11}(t; z + sRD) = s^d R \mathbf{N}_{11}(t; D) R^\top. \quad (46)$$

Furthermore, the singular values of $\mathbf{N}_{11}(t; D)$ fulfills

$$\tau_n(t; z + sRD) = s^d \tau_n(t; D), \quad n = 1 \dots d. \quad (47)$$

We assume for the rest of the paper that the singular values are sorted in a decreasing order: $\tau_1(t; D) \geq \tau_2(t; D) \dots \geq \tau_d(t; D) \geq 0$.

5.2 Shape descriptors based on the polarization tensor

In [2] the authors constructed the GPT-based shape descriptors applicable for the shape identification in electro-sensing. These descriptors have infinite orders and allow to distinguish between complex shapes using only one frequency. Nonetheless, this approach requires high order GPTs (*e.g.*, $\hat{\mathbf{M}}_{mn}(\omega; D)$ for $m, n \geq 2$) which are difficult to obtain in practice, for example with far field and limited angle of measurement view. It has then limited feasibility.

The situation here for the filtered GPTs \mathbf{N} is identical. In fact, the total error of reconstruction at the order K is the sum of the error due to the truncation $O(\rho^{-(K+2)})$ and the error due to the noise $O(\rho^K/N_s)$, with N_s being the number of equally distributed transmitters and $\rho > 1$ the ratio between the transmitter-to-target distance and the size of the target. So the reconstruction of high order information is exponentially unstable, which is contrasted with the fact that at low orders the error due to the noise can be reduced to

zero by increasing the number of transmitters ². Numerical experiments in [4] confirmed that with a large number of transmitters the reconstruction of the polarization tensor (or the first order GPT) is very stable for various settings of measurement system. On the other hand, it is known that the reconstruction of GPTs of order greater than one is extremely unstable when the angle of view is limited [3].

The fundamental limit of using the polarization tensors in shape description is that they do not contain high order information of the shape and can only describe (at a fixed frequency) an equivalent ellipse [9]. However when probed with a range of frequency, distinct shapes have different response which is the basis of the multi-frequency approach proposed in [4]. We propose here a multi-scale construction of shape descriptors in the time domain that exploits the first order filtered polarization tensor \mathbf{N}_{11} at different frequency band by varying the pulse shape h . The new shape descriptors can describe complex shapes and contain both the temporal and frequency signature of a shape. Furthermore, they are particularly robust as we will see in Section 6 by numerical experiments.

5.2.1 Multi-Scale invariants

Assume that h is a band pass filter such that $\hat{h}(0) = 0$ (such function can be easily obtained from derivatives of a Gaussian, for example), and let h_j be the dyadic dilation of h at the scale j :

$$h_j(t) = 2^{j/2}h(2^j t) \quad \text{and} \quad \hat{h}_j(\omega) = 2^{-j/2}\hat{h}(2^{-j}\omega). \quad (48)$$

We choose the normalization here so that the L^2 energy of the pulse remains constant. Figure 1 shows an example of pulse shapes h (smooth truncation of the third derivative of a gaussian) and some scales in the frequency domain.

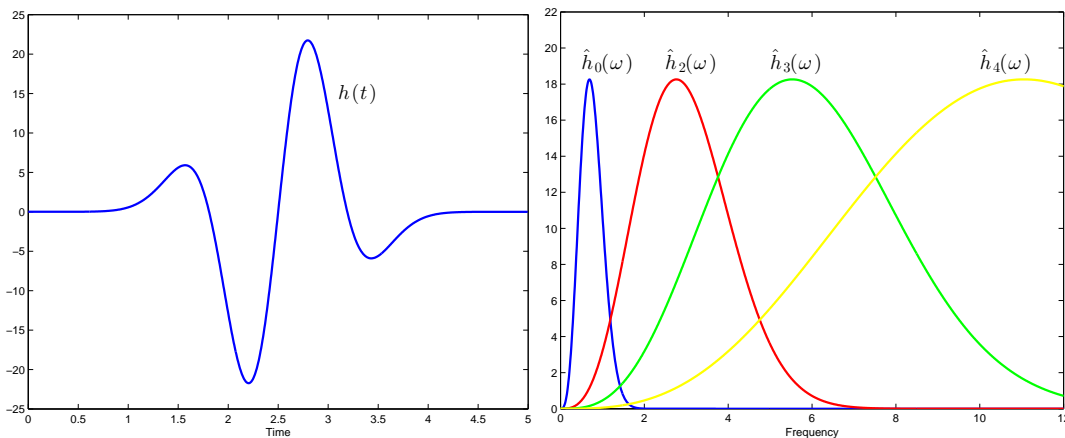


Figure 1: Example of pulse shape h and some Fourier transforms of h_j (rescaled by $2^{j/2}$).

We use h_j as the shape form in the source (14) and acquire for this scale the filtered GPTs $\mathbf{N}_{11}^j(t)$, which is the inverse Fourier transform of $\hat{h}_j(\omega)\hat{\mathbf{M}}_{11}(\omega; D)$. Fix $T > 0$ the

²This is in agreement with the biological evidence that the weakly electric fish's skin is densely covered by the electrical receptors.

duration of signal acquisition at the scale $j = 0$ and define the quantity

$$I_j(t) = I_j(t; D) = \tau_1^j(t; D) \left(\frac{2^j}{T} \int_0^T \|\mathbf{N}_{11}^0(t; D)\|_F^2 dt \right)^{-1/2}, \quad (49)$$

where $\tau_1^j(t; D)$ is the largest singular value of the matrix $\mathbf{N}_{11}^j(t; D)$ and $\|\cdot\|_F$ denotes the Frobenious norm of a matrix. We remark that the definition (49) is always meaningful since $\mathbf{N}_{11}^0(t)$ is a smooth function of t and is not identically zero.

It can be seen easily from Proposition 5.1 that I_j is invariant, in the sense that for arbitrary $z \in \mathbb{R}^d, s > 0, R \in SO(\mathbb{R}^d)$,

$$I_j(t; z + sRD) = I_j(t; D), \quad \forall t > 0. \quad (50)$$

5.2.2 Shape descriptor

In order to be processed numerically, $I_j(t)$ is sampled with the step $\Delta T_j = 2^{-j}T/N$ yielding N equally distributed samples. We set

$$I_{j,n}(D) = I_j(n\Delta T_j; D) \simeq \frac{\tau_1^j(n\Delta T_j; D)}{\left(\frac{2^j}{N} \sum_{n=0}^{N-1} \|\mathbf{N}_{11}^0(n\Delta T_0; D)\|_F \right)^{1/2}}, \quad (51)$$

and use the concatenation $\mathcal{I}(D) := \{I_{j,n}(D)\}_{j,n}$ as the shape descriptor of D . In practice, the number of samples N can be chosen so that the Shannon-Nyquist sampling condition is fulfilled for the (essential) bandwidth of h .

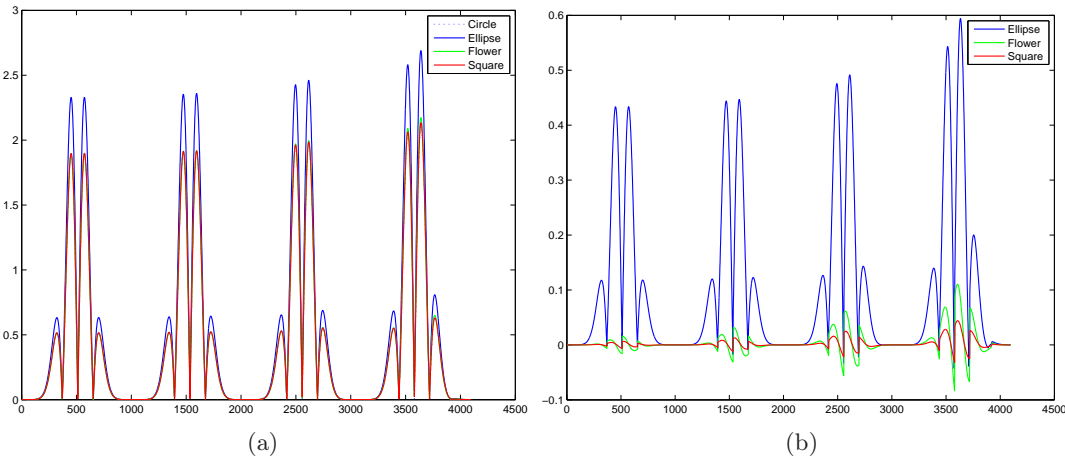


Figure 2: (a): Shape descriptors $\mathcal{I}(D)$ of 4 shapes: Circle, Ellipse, Flower and Square. (b): Difference of the shape descriptor between Circle and the other shapes.

Figure. 2 shows the shape descriptors corresponding to four shapes, computed with the pulse shape in Figure 1.(a) at four consecutive scales $j = -1, 0, 1, 2$. Certain pulse shapes seem to be close to each other and one may ask whether they allow to distinguish shapes with measurement noise. It turns out, as we shall see in the next section, that the reconstruction of

the filtered polarization tensors is well posed and the multi-scale shape descriptors obtained from data are robust even at high noise level. The range of scales $j \in \{j_{\min} \dots j_{\max}\}$ which allows a good distinction between shapes depends on the dictionary and also on the values of σ, ε , and it can be determined in practice by a numerical optimization procedure.

6 Numerical Experiments

We present in this section some numerical results to illustrate the performance of shape identification using pulse-type signals. The pulse shape in Figure 1 is used as h . The acquisition system consists of $N_s = N_r = 50$ positions of transmitters which are distributed on a circle of radius 10.7 and centered at the origin. Each source x_s is composed of two Dirac functions close to each other (within a distance of 0.1) satisfying the condition of neutrality (16). We will consider only the limited view case, *i.e.* the transmitters cover uniformly the angle range $[0, \alpha]$ with $\alpha < 2\pi$, as illustrated by Figure 3. Such a scenario is close to the real world situation (the size of the electric fish's body is comparable to that of the target) and is much harder to solve than the full view case, due to its severe ill-posedness [3].

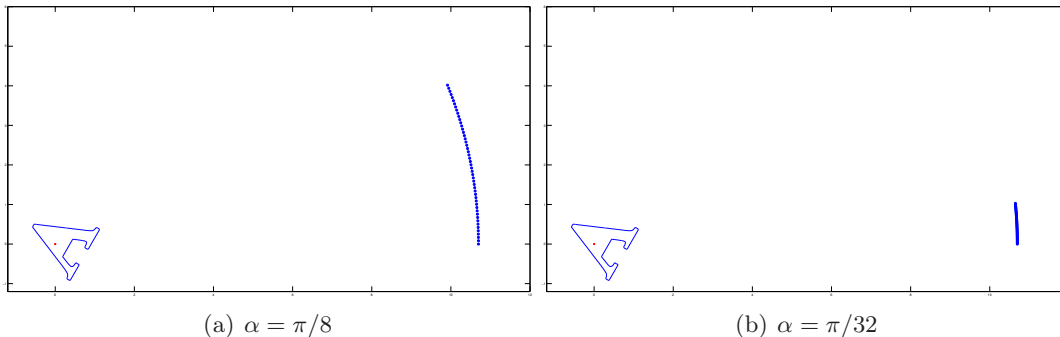


Figure 3: Examples of acquisition system of limited angle of view using 50 transmitters equally distributed on an arc. The center of the target is marked by the red '*'.

The overall procedure of the numerical simulation is resumed as follows.

Dictionary Our dictionary of standard shapes consists of eight elements $\{B_n\}_{n=1\dots 8}$ as shown in Figure 4. All shapes share the same conductivity $\sigma = 10$ and the same permittivity $\varepsilon = 1$, except for the second ellipse which has the electromagnetic parameters $\sigma = 5$ and $\varepsilon = 2$. The conductivity and the permittivity of the background are $\sigma_0 = 1, \varepsilon_0 = 0$. To construct the shape descriptors $\{\mathcal{I}(B_n)\}_n$ of the dictionary, we set h_j as in (48) for four scales $j = -1, 0, 1, 2$ and compute $\mathbf{N}_{11}^j(t; B_n)$ in the frequency domain via (44) and (35), then followed by inverse Fourier transform to go back to the time domain.

Data simulation The same pulse shapes h_j are used for the simulation of data. The target D is one of the dictionary elements after applying the rotation $\theta = \pi/3$, the dilation $s = 1.5$ and the translation $z = [0.1, 0.1]^\top$ with \top being the transpose. At the scale j , the MSR matrix denoted by $\mathbf{V}_j(t)$ is simulated on the time interval $[0, 2^{-j}T]$ with $T = 5$ using $N = 2^9$ uniform samples, by evaluating the integral representation (31). More specifically,

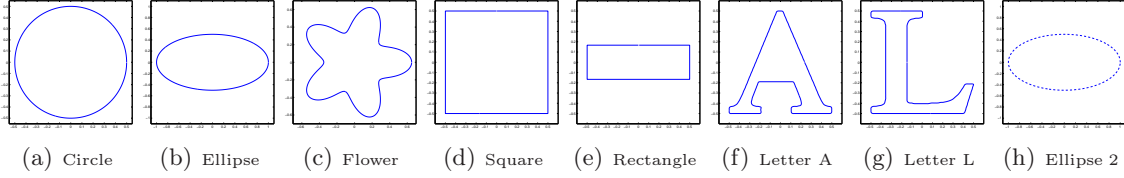


Figure 4: A small dictionary of shapes. All the shapes have the same conductivity $\sigma = 10$ and the same permittivity $\varepsilon = 1$ except the ellipse in dot line which has $\sigma = 5$ and $\varepsilon = 2$.

we first obtain $\varphi(t)$ by solving (32) (with h_j as the pulse shape) via the numerical scheme of Appendix A. Then we apply the single layer potential \mathcal{S}_D on $\varphi(t)$. Further, each entry of the simulated matrix is contaminated by some white noise following the normal distribution $\mathcal{N}(0, \sigma_{\text{noise}}^2)$ with

$$\sigma_{\text{noise}} = \frac{\sigma_{\text{per}}}{\sqrt{N_s N_r}} \left(\frac{1}{2^{-jT}} \int_0^{2^{-jT}} \|\mathbf{V}_j(t)\|_F^2 dt \right)^{-1/2}$$

with σ_{per} being the percentage of the noise. Figure 5 shows the time profile of the entry V_{11} in the MSR matrix for an elliptical target simulated using the pulse shape h_0 .

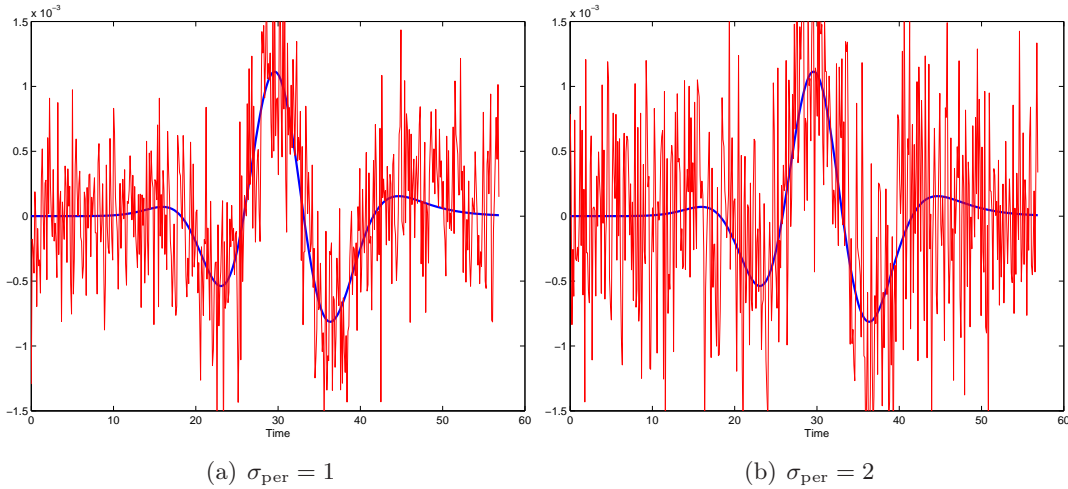


Figure 5: Example of the MSR data $V_{11}(t)$ corresponding to an ellipse. In blue: without noise. In red: with (a) 100% and (b) 200% of noise.

Shape identification For each scale j we reconstruct the filtered polarization tensor $\mathbf{N}_{11}^j(t)$ from the simulated data by inverting the linear system (45) in the time domain (the operator \mathbf{L} is constructed as in (41) with the truncation order $K = 1$). Furthermore, the symmetry of $\mathbf{N}_{11}^j(t)$ is incorporated as a constraint in the inversion in order to enhance the robustness. The shape descriptors are then computed via (51). Finally the euclidean norm

$$\varepsilon(D, B_n) = \|\mathcal{I}(D) - \mathcal{I}(B_n)\|$$

is evaluated for the whole dictionary and the shape is identified as the one yielding the smallest value.

6.1 Results of identification

For each shape of the dictionary, we simulate data and identify it using the procedure described above. Figure 6 shows the results of shape identification for a limited view configuration with the aperture $\alpha = \pi/16$ at two noise levels $\sigma_{\text{per}} = 100\%$ and 200% . The error $\varepsilon(D, B_n)$ is represented here by error bars, where the m -th bar in the n -th group corresponds to $\varepsilon(D, B_m)$ of the identification experiment with the shape D generated by B_n (labeled by its name). The shortest bar in each group is the identified shape and is marked in green, while the true shape is marked in red in case that the identification fails. Each error bar is the average of the same experiment with 100 independent realization of white noise. It can be seen that the identification succeeded for all shapes with 100% of noise, and it failed only for the circle with 200% of noise.

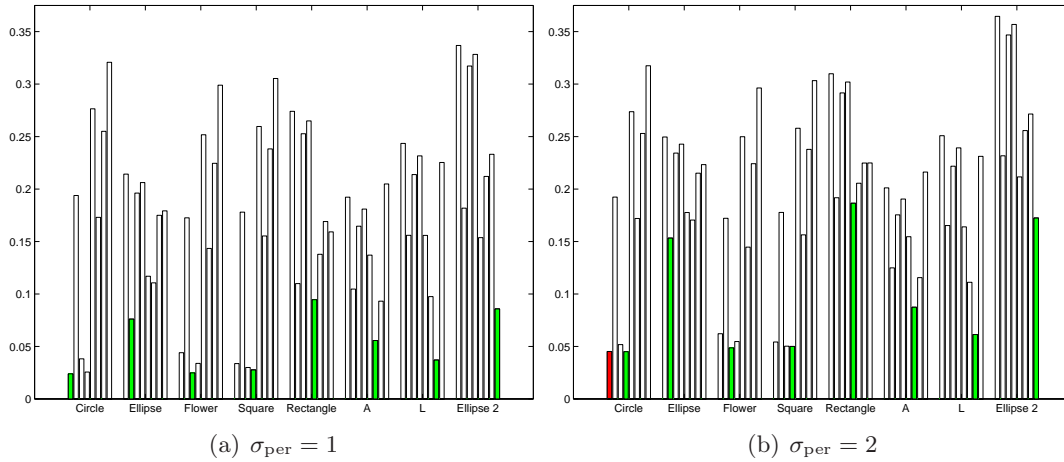


Figure 6: Results of identification at two noise levels using a limited view configuration with the aperture $\alpha = \pi/16$.

Robustness Figure 7 illustrates the robustness of the proposed method in a noisy environment for two settings of limited view with the aperture $\alpha = \pi/8$ and $\alpha = \pi/32$. Each curve represents the probability of successful identification as a function of σ_{per} which ranges from 25% to 800%, obtained by repeating at every noise level the experiment 1000 times with independent realizations of white noise. The horizontal line at 0.125 marks the threshold that the proposed matching method performs better than a random guess. It can be seen that the angle of view can affect the performance, and in both cases all shapes are correctly identified with 100% of noise. It is worth noticing that certain shapes, like the letters and the flower, exhibits an extraordinary robustness.

Number of scales The number of scales has an important impact on the robustness of the identification. A large number of scales contains more information hence gives a better

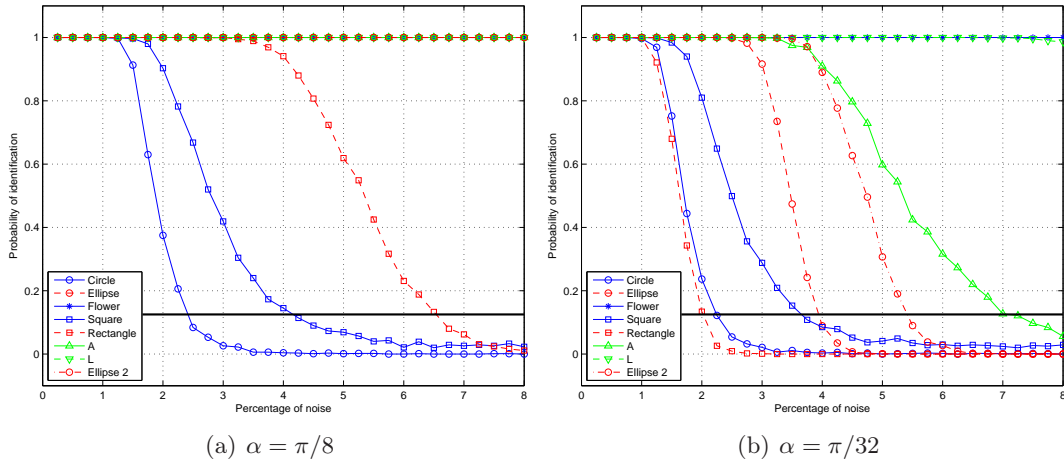


Figure 7: Results of identification at various noise levels with the shape descriptors of 4 scales and the aperture (a): $\alpha = \pi/8$ and (b): $\alpha = \pi/32$.

performance of identification. On the contrary, the overall performance is reduced when the number of scales is insufficient. This can be seen from Figure 8 where the same experiment in Figure 7 is carried out with the scales $j = -1$ and $j = -1, 0$ respectively.

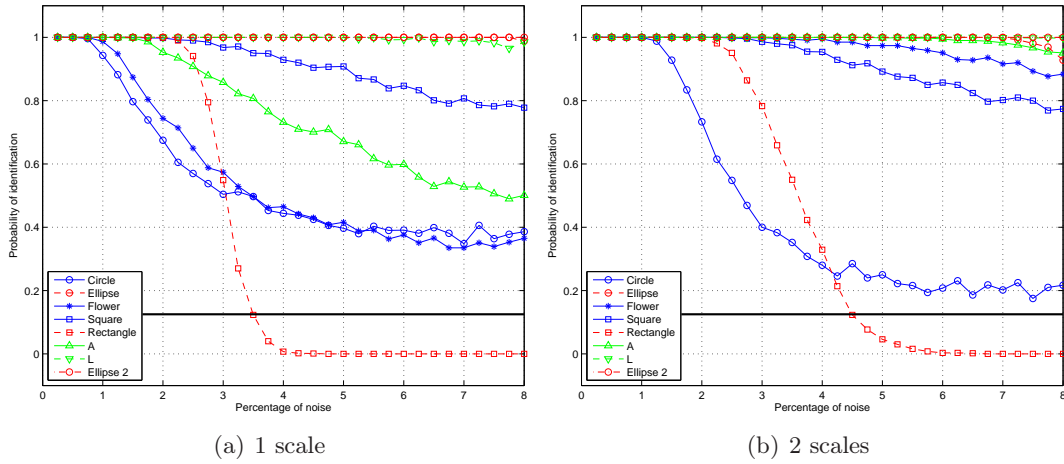


Figure 8: Same experiment as in Figure 7 (a) with the scales (a) $j = -1$ and (b) $j = -1, 0$ only.

7 Discussion and conclusion

In this paper we presented a new time domain multi-scale method of shape identification for electro-sensing using pulse-type signals. The method is based on transform-invariant shape descriptors which are computed from the filtered polarization tensor at multi-scales, and enjoys a remarkable robustness even in a highly noisy environment with far field trans-

mitters of very small angle of view. Time domain data, acquired using pulses of different scales, contain information about the target at different frequency bands, and allow a better distinction of shapes than using a single scale. The new method improves also the results of the multi-frequency approach proposed in [4]. We reported here only results on conductive objects ($\sigma \gg \sigma_0$, compared to the surrounding water), while a similar performance can also be observed on resistive objects ($\sigma \ll \sigma_0$) and in this case one needs to adapt the range of the scales to the new physical values in order to obtain good distinguishability between shapes. The new method can also be generalized to the modeling of electric fish in [1] and this will be the subject of a forthcoming paper. We also plan to optimize the pulse shape for a given dictionary of targets. Finally, it is expected that the proposed time-domain multi-scale algorithm can be extended to shape identification and classification in echolocation [11] and in imaging from induction data [5, 6].

A Numerical solution of the forward problem

We aim to simulate the perturbation $u(t, x) - U(t, x)$ for $t \in [0, T]$ using the representation (31). We will solve the system (32) on the time interval $[0, T]$ under the initial condition $\varphi(0) = 0$ (since φ is causal) by combining a boundary element method (BEM) in space and a finite difference scheme in time.

The time interval $[0, T]$ is equally divided into N parts with the time step $\Delta T = T/N$ and we denote by $\varphi^n(x) = \varphi(n\Delta T, x)$ for $n = 0 \dots N$, so that it holds approximately

$$\varphi'(n\Delta T, x) \simeq \frac{\varphi^n(x) - \varphi^{n-1}(x)}{\Delta T} \quad \text{for a.e. } x \in \partial D.$$

The same discretization in time is applied to term on the right-hand side, $(1 + \alpha\partial_t)\frac{\partial U}{\partial \nu}$, and we write $b = \frac{\partial U}{\partial \nu}$. Inserting these into (32) and after some simple manipulations, we get

$$\left(\tilde{\lambda}I - \mathcal{K}_D^*\right) [\varphi^n] = b^n + \frac{\alpha}{\Delta T + \alpha} \left(\left(\frac{1}{2}I - \mathcal{K}_D^*\right) [\varphi^{n-1}] - b^{n-1} \right) \quad (52)$$

with $\tilde{\lambda} = \frac{\varepsilon/\Delta T + \sigma + 1}{2(\varepsilon/\Delta T + \sigma - 1)}$, and the operator $(\tilde{\lambda}I - \mathcal{K}_D^*)$ is clearly invertible on $L^2(\partial D)$. In the space domain (with the time being fixed), \mathbb{P}_0 elements are used for the discretization of $L^2(\partial D)$ function. Let $x(\theta)$ be the parameterization of the boundary ∂D with $\theta \in [0, 1]$. We denote by $\varphi_j^n = \varphi(n\Delta T, x(\theta_j))$ the j -th coefficient of $\varphi(n\Delta T)$ under the \mathbb{P}_0 basis, and by $A_{\tilde{\lambda}}, A_{1/2}$ the matrix representation of $(\tilde{\lambda}I - \mathcal{K}_D^*), (\frac{1}{2}I - \mathcal{K}_D^*)$ under $\mathbb{P}_0 \times \mathbb{P}_0$ basis. Denoting by $\boldsymbol{\varphi}^n = (\varphi_j^n)_j, \mathbf{b}^n = (b_j^n)_j$ the discrete coefficient vector, finally the time-space discretization yields the following linear system for $n = 1 \dots N$:

$$A_{\tilde{\lambda}}\boldsymbol{\varphi}^n = \mathbf{b}^n + \frac{\alpha}{\Delta T + \alpha} (A_{1/2}\boldsymbol{\varphi}^{n-1} - \mathbf{b}^{n-1}) \quad (53)$$

with the initial state $\boldsymbol{\varphi}^0 = 0$. Then (53) is inverted iteratively for $n = 1 \dots N$ and we inject the solution $\{\boldsymbol{\varphi}^0, \dots, \boldsymbol{\varphi}^n\}$ into (31) to get the desired data by evaluating the single layer potential.

References

- [1] H. Ammari, T. Boulier, and J. Garnier. Modeling active electrolocation in weakly electric fish. *SIAM J. Imag. Sci.*, 6(1):285–321, 2013. [2](#), [3](#), [6](#), [14](#), [21](#)
- [2] H. Ammari, T. Boulier, J. Garnier, W. Jing, H. Kang, and H. Wang. Target identification using dictionary matching of generalized polarization tensors. *Found. Comput. Math.*, 14(1):27–62, February 2014. [11](#), [12](#), [13](#), [14](#)
- [3] H. Ammari, T. Boulier, J. Garnier, H. Kang, and H. Wang. Tracking of a mobile target using generalized polarization tensors. *SIAM J. Imag. Sci.*, 6(3):1477–1498, August 2013. [15](#), [17](#)
- [4] H. Ammari, T. Boulier, J. Garnier, and H. Wang. Shape recognition and classification in electro-sensing. *Proc. Natl. Acad. Sci. USA*, 111(32):11652–11657, August 2014. [2](#), [3](#), [6](#), [14](#), [15](#), [21](#)
- [5] H. Ammari, J. Chen, Z. Chen, J. Garnier, and D. Volkov. Target detection and characterization from electromagnetic induction data. *J. Math. Pures Appl.*, 101:54–75, 2014. [21](#)
- [6] H. Ammari, J. Chen, Z. Chen, D. Volkov, and H. Wang. Detection and classification from electromagnetic induction data. *arXiv:1308.6027*, 2014. [21](#)
- [7] H. Ammari, D. Chung, H. Kang, and H. Wang. Invariance properties of generalized polarization tensors and design of shape descriptors in three dimensions. *Appl. Comput. Harmonic Anal.*, 2014. [11](#)
- [8] H. Ammari, J. Garnier, W. Jing, H. Kang, M. Lim, K. Solna, and H. Wang. *Mathematical and Statistical Methods for Multistatic Imaging*. Lecture Notes in Mathematics. Springer Verlag, 2013. [7](#)
- [9] H. Ammari and H. Kang. *Polarization and moment tensors: with applications to inverse problems and effective medium theory*, volume 162. Springer Verlag, New York, 2007. [15](#)
- [10] H. Ammari, H. Kang, H. Lee, and M. Lim. Enhancement of near cloaking using generalized polarization tensors vanishing structures. part i: The conductivity problem. *Comm. Math. Phys.*, 317(1):253–266, 2013. [11](#)
- [11] H. Ammari, M.P. Tran, and H. Wang. Shape identification and classification in echolocation. *SIAM J. Imag. Sci.*, 2014. [21](#)
- [12] J. Bastian. Electrolocation i. how the electroreceptors of *apteronotus albifrons* code for moving objects and other electrical stimuli. *J Comp. Physiol. A*, 144:397–411, 1981. [1](#)
- [13] R. Budelli and A.A. Caputi. The electric image in weakly electric fish: perception of objects of complex impedance. *J. Exp. Bio.*, 203(3):481, 2000. [1](#)

- [14] O.M. Curet, N.A. Patankar, G.V. Lauder, and M.A. MacIver. Aquatic maneuvering with counter-propagating waves: a novel locomotive strategy. *J. Royal Soc. Interface*, 8:1041–1050, 2010. [1](#)
- [15] H.W. Lissmann and K.E. Machin. The mechanism of object location in *Gymnarchus niloticus* and similar fish. *J. Exp. Bio.*, 35(2):451–486, 1958. [1](#)
- [16] M.A. Maciver. *The computational neuroethology of weakly electric fish: body modeling, motion analysis, and sensory signal estimation*. PhD thesis, Citeseer, 2001. [1](#)
- [17] M.A. MacIver, N.M. Sharabash, and M.E. Nelson. Prey-capture behavior in gymnotid electric fish: motion analysis and effects of water conductivity. *J. Exp. Bio.*, 204(3):543–557, 2001. [1](#)
- [18] P. Moller. *Electric fish: history and behavior*. Chapman and Hall, London, 1995. [1](#)
- [19] I.D. Neveln, Y. Bai, J.B. Snyder, , J.R. Solberg, O.M. Curet, K.M. Lynch, and M.A. MacIver. Biomimetic and bio-inspired robotics in electric fish research. *J. Exp. Biology*, 216:2501–2514, 2013. [1](#)
- [20] J.R. Solberg, K.M. Lynch, and M.A. MacIver. Active electrolocation for underwater target localization. *Internat. J. Robotics Res.*, 27(5):529–548, 2008. [1](#)
- [21] G. von der Emde. Active electrolocation of objects in weakly electric fish. *J. Exp. Bio.*, 202(10):1205–1215, 1999. [1](#)
- [22] G. von der Emde. Distance and shape: perception of the 3-dimensional world by weakly electric fish. *J. Physiol. Paris*, 98:67–80, 2004. [1](#)
- [23] G. von der Emde. Non-visual environmental imaging and object detection through active electrolocation in weakly electric fish. *J. Comp. Physiol A*, 192:601–612, 2006. [1](#)
- [24] G. von der Emde and S. Fetz. Distance, shape and more: recognition of object features during active electrolocation in a weakly electric fish. *J. Exp. Bio.*, 210(17):3082–3095, 2007. [1](#)
- [25] G. von der Emde and T. Ringer. Electrolocation of capacitive objects in four species of pulse-type weakly electric fish i. discrimination performance. *Ethology*, 91(4):326–338, 1992. [1](#)
- [26] G. von der Emde, S. Schwarz, L. Gomez, R. Budelli, and K. Grant. Electric fish measure distance in the dark. *Science*, 260:1617–1623, 1993. [1](#)